Estimating Asteroid Mass from Optically Tracked Radio Beacons

Lukas Christensen[*]
Technical University of Denmark, 2800 Kongens Lyngby, Denmark
Ryan S. Park[†]
Jet Propulsion Laboratory, California Institute of Technology, Pasadena, California 91109
and
James F. Bell, III[‡]
Arizona State University, Tempe, Arizona 85281

https://doi.org/10.2514/1.A34830

This Paper presents the feasibility of estimating the mass of an asteroid by tracking a number of probes ejected from a host spacecraft during a flyby. The probes are designed to fly by at a much closer distance to the asteroid than the host spacecraft, which lowers the risk of endangering the overall mission. The motion of these probes is perturbed due to the target asteroid's mass, and by tracking the probes from the host spacecraft, the change in relative separation between the probes, which is directly proportional to the asteroid's mass, can be measured with high precision. The probes are small reflective spheres that are tracked by an imager mounted on the spacecraft; however, the addition of radio transceivers inside the probes can greatly enhance the mass-recovery performance. A hypothetical mission to a main-belt asteroid with the physical characteristics of (101955) Bennu is used as a reference, and an extensive covariance analysis is performed to determine the recoverable mass accuracy under various conditions. The result shows that, under realistic assumptions, the mass of a Bennu-like asteroid can be recovered with a 1σ accuracy better than 20% from optical tracking. In case radio transceivers are considered, the recovered asteroid mass accuracy reduces to better than 5%.

Nomenclature

A	=	Jacobian of state update function
B	=	process noise mapping matrix
b	=	information vector
C	=	rotation matrix of spacecraft
$C_{\mathrm{RP,jk}}$	=	radiation pressure constant for k acting on j, $\mathrm{m^3/s^2}$
F	=	state update function
G	=	measurement function
H	=	Jacobian of measurement function
K	=	matrix of intrinsic camera parameters
N	=	number of probes
n_j	=	unmodeled acceleration for j, $\mathrm{m/s^2}$
P	=	covariance matrix
P_w	=	noise covariance matrix
R	=	square root information matrix
$r_j, \dot{r}_j, \ddot{r}_j$	=	position, velocity, and acceleration of j relative to solar system barycenter, m, m/s, and $\mathrm{m/s^2}$, respectively
$r_{\mathrm{jk}}, \dot{r}_{\mathrm{jk}}, \ddot{r}_{\mathrm{jk}}$	=	position, velocity, and acceleration of j relative to k, m, m/s, and $\mathrm{m/s^2}$, respectively
T_H	=	orthogonal Householder transformation matrix
t_0, t_e, t, t_l	=	initial, ejection, variable, and specific time, s
u_j, v_j	=	normalized camera coordinates of j
u_j', v_j', w_j	=	camera coordinates of j
V	=	square root measurement covariance
W	=	measurement covariance matrix
X	=	true state vector
X^*	=	reference state vector
X_j	=	state subvector for j
Y	=	measurement vector
Z_j	=	measurement subvector for j
β_s	=	ecliptic latitude of spacecraft, rad
Δt_i	=	probe oscillator phase offset, s
$\Delta \dot{t}_i$	=	probe oscillator frequency offset
δX	=	state deviation vector
δY	=	measurement deviation vector
ϵ	=	error term vector
θ	=	probe ejection angle, rad
λ_s	=	ecliptic longitude of spacecraft, rad
μ_k	=	gravitational parameter of k
$\rho_s, \dot{\rho}_s$	=	range and Doppler rate between tracking station and spacecraft, m and m/s, respectively
$\rho_i, \dot{\rho}_i$	=	range and Doppler rate between spacecraft and probe, m and m/s, respectively
ϱ_{ij}	=	range between probe i and probe j, m/s
σ_{ss}	=	steady-state stochastic accelerations, $\mathrm{m/s^2}$
τ	=	noise correlation time, s
Φ	=	state transition matrix
ϕ	=	probe observation angle, rad
ψ_s	=	spacecraft rotation angles, rad

Subscripts

a	=	asteroid
c	=	camera
i	=	individual probe
o	=	tracking station
p	=	all probes combined
s	=	spacecraft
$\odot$	=	sun
$\oplus$	=	Earth

*Postdoc, Division of Measurement and Instrumentation Systems, DTU Space, Elektrovej 327.
†Group Supervisor, Mission Design and Navigation Section, 4800 Oak Grove Drive. Associate Fellow AIAA.
‡Professor, School of Earth and Space Exploration, 781 Terrace Mall.

I. Introduction

K NOWING the masses of asteroids throughout the solar system greatly benefits several disciplines such as planetary defense and planetary science. However, for most of the asteroids in the solar system, the mass is an unknown quantity and is typically constrained based on its spectral type. In the few cases where the mass has been

determined (without the benefit of a close spacecraft flyby or orbital rendezvous), the recovered accuracy is typically poor, mainly due to large uncertainties in the input variables that enabled the estimate.

The size of an asteroid can relatively easily be estimated based on its brightness and knowing its approximate reflectivity, which can be determined from its spectral class [1]. The spectral class also determines the approximate density, and hence its mass can be estimated. However, the size estimate is not particularly precise, and this method therefore generally leads to high mass uncertainties [2].

The value can be improved by observing disturbances to the orbits of other objects in the solar system and then performing extensive calculations [3,4] to extract the contributions caused by the asteroid's gravity. In these calculations, it is commonly assumed that the orbital parameters of the perturbing asteroid are known quantities; however, because the objects under consideration are gravitationally coupled, this approximation will in some cases lead to significant errors in the mass estimate and must therefore be accounted for [5]. In general, this approach requires either a relatively heavy asteroid or close encounters with the other objects in order to produce orbital deflections that can be successfully measured and decoupled from other disturbances. Mass precision on the scale of 5% is achievable with this method, but it is limited to the asteroids which satisfy the limiting conditions of being sufficiently large and in an appropriate orbital configurations with all main belt asteroids processed with this method having masses in excess of 10^{14} kg [6].

If better precision is required, a solution is to have a spacecraft rendezvous with the asteroid and either fly by or orbit around it. With the orbital approach, the mass can be determined with an uncertainty of less than 1% [7], whereas the precision achievable during a flyby depends greatly on the specifics of the object as well as the flyby and tracking geometry. For small asteroids, the spacecraft will have to pass perilously close by the asteroid in order to achieve a significant deflection that can be uncoupled from other disturbances such as solar radiation pressure. Furthermore, before the encounter, the position of the asteroid will generally only be determined to within a few kilometers, which further complicates the recovery of mass from a flyby. However, this issue can be alleviated by tracking the asteroid from the spacecraft during the approach phase. It is also possible to improve results by having multiple spacecraft flying in formation either during flybys [8,9] or in orbit around the target [10].

This Paper presents a possible solution to improve the mass recovery from a flyby by deploying a series of probes which can provide the following benefits:

1) Such probes can be made to approach the asteroid at much closer distances without endangering the spacecraft, thus providing increased deflection.

2) The relatively short distances between the probes and the spacecraft will allow for more precise observations compared to the Earth-based tracking of the spacecraft.

3) By having the probes approach the asteroid at different distances and/or from different directions, the differential deflection of their trajectories can be used to pinpoint the mass of the asteroid, even though its position is not well determined.

4) If the probes are constructed with adequate uniformity, it can reasonably be assumed that any external disturbances will affect them equally, thus allowing for such disturbances to be decoupled from the gravity of the asteroid. Solar radiation pressure will, for example, result in an acceleration term that is approximately equal for all probes, whereas asteroid gravity will affect them differently. By looking at the difference between the probes, solar radiation pressure will thus disappear while gravity is retained.

The probes can, in principle, be as simple as small inert spheres coated in a highly reflective material that allows them to be imaged from large distances for angles-only camera measurements.

The Johns Hopkins University Applied Physics Laboratory has proposed a concept, called OpGrav [11], that uses the described probe based measurement method, and has successfully demonstrated probe deployment with the Small Body In-Situ Multi-Probe Mass Estimation Experiment project [12]. The work has mainly been focused on image-based measurements using cameras from previous missions as a baseline for their design. The disadvantage of using only onboard imaging is that the uncertainty associated with measuring the deflection of probe trajectories caused by the asteroid is directly proportional to the distance between the spacecraft and the probes. This limits the attainable mass estimation accuracy, especially for large flyby distances.

The use of deployable probes for spacecraft in orbit around a target body has also been suggested in the literature [13,14]. Such configurations can potentially be used to estimate not only the bulk density of the target but also spherical harmonic coefficients describing the gravitational field, as has been demonstrated using naturally occurring probes around asteroid (101955) Bennu [15].

This Paper examines how the OpGrav concept might be improved by extending the probe design to include radio transceivers. Three measurement methods are considered: one using only imaging, one using Doppler measurements to estimate radial probe speed relative to the spacecraft, and one using time of flight (i.e., ranging) to measure the distances between the probes and the spacecraft as well as the distances between the probes themselves.

In Sec. II, a reference scenario will be introduced that is used to characterize the potential performance of the measurement principle. Sections III and IV describe the theory used for modeling the dynamics of the reference scenario and for evaluating performance. Results of the analysis are presented in Sec. V, and some practical considerations are discussed in Sec. VI.

II. Reference Mission

To evaluate the performance of the mass estimation methods, a reference mission has been constructed where, as illustrated in Fig. 1, a spacecraft is launched into a elliptical orbit around the sun and encounters a main belt asteroid at aphelion. The initial position of the asteroid and the exact parameters of the spacecraft orbit are selected such that they result in a minimum flyby distance equal to 50 km. Before the encounter, the spacecraft ejects a number of probes at speeds and ejection directions selected such that, at the encounter, the probes form a circle around the asteroid with its normal vector parallel to the asteroid's direction of travel. Specifics of the orbit are as follows: the spacecraft is in an elliptical 1 AU by 2.5 AU orbit; the asteroid is in a 2.5 AU orbit; the flyby distance is equal to 50 km; the flyby speed is 4.6 km/s; and the approach distance is 1 km. All orbits are considered to be coplanar and aligned with the ecliptic, with the Earth's and the asteroid's orbits being circular.

Approach and flyby distance are defined as the minimum distance to the asteroid from the probes and the spacecraft, respectively. The asteroid is modeled after (101955) Bennu, and the physical parameters of it and those of the other involved objects are shown in Table 1 [16,17]. GM is the standard gravitational parameter. Note that the first value given for the probe information represents the OpGrav and OpRange scenarios, whereas the second value represents the OpDoppler scenario. All objects are assumed to be spherical.
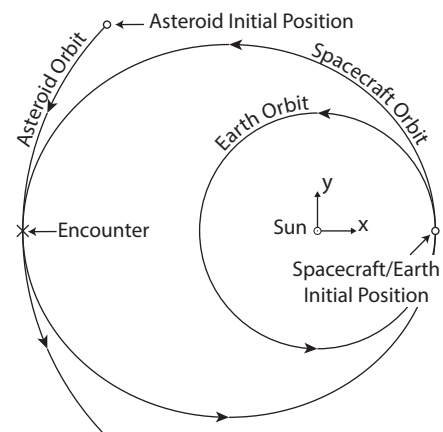

Fig. 1 The orbital setup of the reference mission in sun-centric coordinates.

**Table 1   Object parameters of the main spacecraft and the probes**

Object parameter	Asteroid	Spacecraft	Probe
Diameter	490 m [7]	1 m	15 cm, 50 cm
Mass	7.329×10^{10} kg [16]	500 kg	1 kg, 20 kg
GM	4.892 m^3/s^2 [16]	3.3×10^{-8} m^3/s^2	——
$\bar{J}_2$	−0.017511 [17]	——	——
Albedo	0.043 [7]	0.5	0.85
Count	1	1	3,1

Three scenarios are considered: the OpGrav method, the OpRange method, and the OpDoppler method.

In the OpGrav method, a total of three probes are ejected and tracked as they move toward the approach points. The concept is illustrated in Fig. 2. A camera mounted on the spacecraft is used to track the angular motion of the probes as well as that of the asteroid.

The OpRange method, depicted in Fig. 3, uses a similar mission profile, but with the addition of radio transceivers being built into the probes. These beacons each transmit a radio signal at specified intervals, which is then picked up by the other probes as well as by the spacecraft. By determining the arrival times of these signals, the probe–spacecraft distances as well as the probe–probe distances can be estimated. It is assumed that physical constraints will limit arrival time estimation precision to a few nanoseconds using one-way radio links and that, in addition, differences in oscillator hardware will cause the range estimates to be offset from the true value as well as to drift over time. These issues are mitigated by incorporating correcting terms in the state vector during data processing. Achieving this level of precision with the probe form factor might not be a trivial matter and is discussed further in Sec. VI.

The OpDoppler method is based on the GRAIL and GRACE missions, which use ultrastable oscillators and two-way radio links to achieve highly accurate radial velocity measurements between two satellites [18,19]. This scenario, as shown in Fig. 4, uses a similar concept, combined with optical tracking, to track the trajectory of a single probe as it encounters the asteroid. This approach requires significantly more complex hardware compared to the other methods, and it was therefore decided to reduce the number of probes to 1, as this was deemed to represent a more achievable mission scenario.
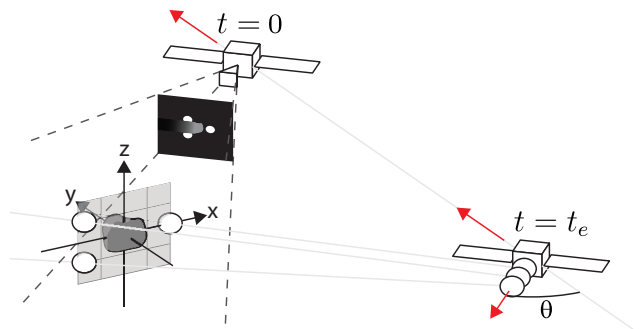
Fig. 2   Illustration of the OpGrav method; t_e is the time of ejection, and $t = 0$ is the time of closest approach.
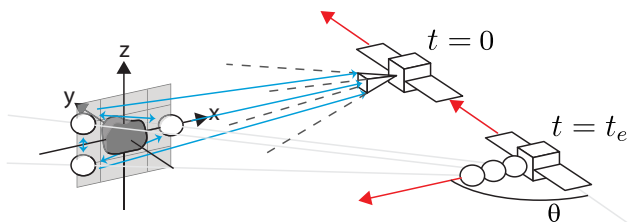
Fig. 3   Illustration of the OpRange method; t_e is the time of ejection, and $t = 0$ is the time of closest approach.
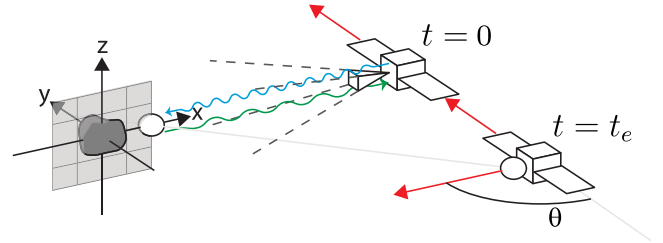
Fig. 4   Illustration of the OpDoppler method; t_e is the time of ejection, and $t = 0$ is the time of closest approach.

Regardless, this method will be challenging to implement in practice as will be discussed in Sec. VI.

Common for all scenarios is that the spacecraft is tracked from an Earth-based tracking station using X-band radio. Measurements are performed once per hour with the camera pointed toward the probes for most of the encounter; however, from one day before until one day after the time of closest approach, the camera is instead pointed toward the asteroid. This is done to allow for science operations as well as to improve the positional estimate of the asteroid. In addition, during the closest approach ($|t| < 1$ h), the measurement rate is increased to once per minute in order to better capture the dynamics of the encounter. Normal observations then continue for 7 days after the closest approach.

The camera measurements are based on the Advanced Pointing Imaging Camera (APIC) [20], which is a high-resolution imaging system developed at the Jet Propulsion Laboratory consisting of two cameras (one narrow angle and one wide angle) mounted on a two degree-of-freedom (DOF) actuation platform. Because the relative orientation of the two cameras is known with a high precision, the platform is capable of providing accurate pointing information by simultaneously having one camera observe a target, while the other captures a star field. Furthermore, the two DOF actuation makes the system well suited for imaging targets moving at high relative speeds as it reduces the need for reorienting the entire spacecraft, thus making it ideal for this type of mission.

III.   Covariance Analysis

To estimate the attainable observation uncertainty of the mass determination method, a square root information batch processor [21] has been implemented. In general, the approach estimates the values of an initial state vector given a series of measurements by linearizing the system dynamics around a reference trajectory and then iteratively adjusting the reference until the system converges. The covariance matrix associated with the state vector is simultaneously estimated and can be used to determine the precision of the state vector estimate [22–26].

A.   Algorithm Overview

The algorithm processes an observation at time t_l by first integrating a reference trajectory from t_{l-1} to t_l and then calculating the Jacobian $\boldsymbol{H}$ of the measurement function with respect to the state vector, evaluated on the reference trajectory:

$$H(t_l) = \left[\frac{\partial G(X(t), t)}{\partial X(t)} \right]_{X^*(t_l)} \quad (1)$$

where $\boldsymbol{G}(\boldsymbol{X}(t), t)$ is the measurement function and $\boldsymbol{X}^*(t_l)$ is the calculated reference state. This is then related to the initial state at t_0, rather than the current state, by means of

$$H(t_0|t_l) = H(t_l)\Phi(t_l, t_0) \quad (2)$$

with $\boldsymbol{\Phi}(t_l, t_0)$ being the state transition matrix (STM) at time t_l. The STM is determined simultaneously with the reference state through numerical integration and is governed by the differential equation

$$\mathbf{\Phi}(t_0, t_0) = \mathbf{I}, \quad \dot{\mathbf{\Phi}}(t, t_0) = \mathbf{A}(t)\mathbf{\Phi}(t, t_0) \tag{3}$$

where

$$\mathbf{A}(t) = \left[\frac{\partial \mathbf{F}(\mathbf{X}(t), t)}{\partial \mathbf{X}(t)}\right]_{\mathbf{X}^*(t)} \tag{4}$$

is the Jacobian of the state update function $\mathbf{F}(\mathbf{X}(t), t)$ with respect to the state vector, evaluated on the reference state. To improve numerical performance, the algorithm operates on the square root information matrix $\mathbf{R}(t)$, defined by

$$\mathbf{R}^{\mathsf{T}}(t)\mathbf{R}(t) = \mathbf{\Lambda}(t) = \mathbf{P}^{-1}(t) \tag{5}$$

rather than the covariance matrix $\mathbf{P}$ directly. Similarly, instead of the state deviation vector $\delta \mathbf{X}(t)$, the information vector

$$\mathbf{b}(t) = \mathbf{R}(t)\delta \mathbf{X}(t) \tag{6}$$

is used. These quantities are updated using the modified measurement Jacobian according to

$$\mathbf{T}_H \begin{bmatrix} \mathbf{R}(t_0|t_0, \dots, t_{l-1}) & \mathbf{b}(t_0|t_0, \dots, t_{l-1}) \\ \mathbf{V}^{-1}(t_l)\mathbf{H}(t_0|t_l) & \mathbf{V}^{-1}(t_l)\delta \mathbf{Y}_l \end{bmatrix}$$
$$= \begin{bmatrix} \mathbf{R}(t_0|t_0, \dots, t_l) & \mathbf{b}(t_0|t_0, \dots, t_l) \\ \mathbf{0} & \boldsymbol{\epsilon}_l \end{bmatrix} \tag{7}$$

where $\mathbf{T}_H$ is a Householder transformation that produces an upper triangular matrix; $\delta \mathbf{Y}_l = \mathbf{Y}(t_l) - \mathbf{G}(\mathbf{X}(t_l), t_l)$ is the difference between the actual observations and the expected observations based on the reference trajectory; $\boldsymbol{\epsilon}_i$ is an error term; and $\mathbf{V}(t_l)$ is defined by

$$\mathbf{V}(t_l)\mathbf{V}^{\mathsf{T}}(t_l) = \mathbf{W}(t_l) \tag{8}$$

with $\mathbf{W}(t_l)$ being the measurement covariance matrix.

This process is repeated for all measurements $1, \dots, M$, after which the state deviation vector incorporating all the available data $\delta \mathbf{X}(t_0|t_0, \dots, t_M)$ is calculated and used to update the reference trajectory according to

$$\mathbf{X}^*(t_0) = \mathbf{X}^*(t_0) + \delta \mathbf{X}(t_0|t_0, \dots, t_M) \tag{9}$$

The process is then repeated until $\mathbf{X}^*(t_0)$ converges to a constant value. Finally, $\mathbf{P}(t_0|t_0, \dots, t_M)$ is calculated, thus describing the covariance associated with final state estimate [27].

B. Stochastic Effects

The effects of forces not included in the acceleration model can be investigated by adding time correlated stochastic process noise to the system. Because the batch processing algorithm only determines the state at t_0, it implicitly assumes that any such disturbances are constant, which is not a realistic assumption. To account for this, the processing can be split up into smaller batches, each representing a time span shorter than the correlation time of the process noise,

and then the initial state for each batch can be estimated [27]. This effectively models the stochastic acceleration as being a piecewise constant function, which better represents the disturbances. However, this will likely require smoothing to produce consistent results because the different batches are treated individually. A similar outcome can be achieved while still only estimating the state at t_0 by extending the state vector to include bias terms representing the unmodeled acceleration for each of the time spans represented by the batches and then updating the state transition matrix to point to the appropriate bias term for any given time. By doing it this way, no smoothing is needed as information about the entire trajectory is available to the estimator.

Because unmodeled forces affect the square root information matrix in a way that the described batch processing algorithm does not account for, the state uncertainty will generally be underestimated if such effects are added. To address this issue, the algorithm must be modified to determine $\mathbf{R}(t_l|t_0, \dots, t_l)$ rather than $\mathbf{R}(t_0|t_0, \dots, t_l)$. For each measurement l, this can be achieved by integrating

$$\dot{\mathbf{R}}(t) = -\mathbf{R}(t)\mathbf{A}(t) - \frac{1}{2}\mathbf{R}(t)\mathbf{B}\mathbf{P}_\omega\mathbf{B}\mathbf{R}^{\mathsf{T}}(t)\mathbf{R}(t) \tag{10}$$

from t_{l-1} to t_l with initial condition $\mathbf{R}(t_{l-1}|t_0, \dots, t_{l-1})$ resulting in $\mathbf{R}(t_l|t_0, \dots, t_{l-1})$ and then performing the measurement update according to

$$\mathbf{T}_H \begin{bmatrix} \mathbf{R}(t_l|t_0, \dots, t_{l-1}) & \mathbf{b}(t_l|t_0, \dots, t_{l-1}) \\ \mathbf{V}^{-1}(t_l)\mathbf{H}(t_l) & \mathbf{V}^{-1}(t_l)\delta \mathbf{Y}_l \end{bmatrix}$$
$$= \begin{bmatrix} \mathbf{R}(t_l|t_0, \dots, t_l) & \mathbf{b}(t_l|t_0, \dots, t_l) \\ \mathbf{0} & \boldsymbol{\epsilon}_i \end{bmatrix} \tag{11}$$

rather than according to Eq. (7). Here, $\mathbf{B}$ is a matrix that describes how the process noise maps to the system, and

$$\mathbf{P}_w = 2\tau\sigma_{ss}^2\mathbf{I} \tag{12}$$

is a matrix describing the characteristics of the noise, with τ being the correlation time and σ_{ss} being its standard deviation [28].

IV. State Space Model

For the sake of simplicity, the spacecraft is considered to only be affected by solar gravity, solar radiation pressure, and asteroid gravity, whereas the asteroid is only affected by solar gravity. The forces considered as acting on the probes are solar gravity, solar radiation pressure, asteroid gravity, asteroid J_2 disturbance, asteroid radiation pressure, spacecraft gravity, and spacecraft radiation pressure. The effects these forces have on the trajectory of the probes are illustrated in Table 2. The probe orbits are clearly dominated by solar effects and the asteroid gravity term, as would be expected, whereas effects of asteroid radiation pressure and the J_2 term are insignificant in comparison. Both spacecraft gravity and radiation pressure cause significant displacements; however, because these forces only affect the probes to a measurable degree immediately after probe ejection, the effects are indistinguishable from errors in ejection speed. Because of this, only solar gravity, solar radiation pressure, and asteroid gravity are included in the state space model used for estimating asteroid mass; however, all the forces of the table are used when generating ground truth trajectories.

Table 2   Effect of forces considered for the probes

Cause	Peak acceleration, km/s^2	Velocity change, km/s	Displacement, km
Solar gravity	9.5×10^{-7}	1.7	1.5×10^6
Solar radiation pressure	1.8×10^{-12}	3.2×10^{-5}	2.9×10^1
Asteroid gravity	4.9×10^{-9}	2.1×10^{-9}	1.3×10^{-3}
Spacecraft gravity	3.3×10^{-11}	5.1×10^{-10}	9.1×10^{-4}
Spacecraft radiation pressure	6.4×10^{-12}	9.7×10^{-11}	1.2×10^{-4}
Asteroid J_2	7.7×10^{-12}	2.4×10^{-12}	1.4×10^{-6}
Asteroid radiation pressure	1.2×10^{-14}	5.3×10^{-15}	3.2×10^{-9}

A. Governing Equations of Motion

The acceleration caused by an object k on an object j is modeled as

$$\ddot{\boldsymbol{r}}_{jk} = -\mu_k \frac{\boldsymbol{r}_{jk}}{|\boldsymbol{r}_{jk}|^3} + \boldsymbol{a}_{RPjk} \qquad (13)$$

where μ_k is the gravitational parameter of object k, $\boldsymbol{r}_{jk}$ is the position vector of object j relative to object k, and $\boldsymbol{a}_{RPjk}$ is the acceleration caused by radiation pressure. Because all objects are considered to be spheres with uniform reflectivity, this can be rewritten as

$$\ddot{\boldsymbol{r}}_{jk} = (C_{RP,jk} - \mu_k) \frac{\boldsymbol{r}_{jk}}{|\boldsymbol{r}_{jk}|^3} \qquad (14)$$

where $C_{RP,jk}$ is a constant that depends on the specifics of the object [29].

The modeled acceleration of the objects under consideration can now be written as

$$\ddot{\boldsymbol{r}}_a = -\mu_\odot \frac{\boldsymbol{r}_a}{|\boldsymbol{r}_a|^3} \qquad (15)$$

for the asteroid,

$$\ddot{\boldsymbol{r}}_s = (C_{RP,s\odot} - \mu_\odot) \frac{\boldsymbol{r}_{s\odot}}{|\boldsymbol{r}_{s\odot}|^3} - \mu_a \frac{\boldsymbol{r}_{sa}}{|\boldsymbol{r}_{sa}|^3} + \boldsymbol{n}_s \qquad (16)$$

for the spacecraft, and

$$\ddot{\boldsymbol{r}}_i = (C_{RP,i\odot} - \mu_\odot) \frac{\boldsymbol{r}_{i\odot}}{|\boldsymbol{r}_{i\odot}|^3} - \mu_a \frac{\boldsymbol{r}_{ia}}{|\boldsymbol{r}_{ia}|^3} + \boldsymbol{n}_i \qquad (17)$$

for the ith probe; $\mu_\odot$ and μ_a are the gravitational parameters of, respectively, the sun and the asteroid, and $\boldsymbol{n}_s$ and $\boldsymbol{n}_i$ are bias terms corresponding to unmodeled acceleration. It is assumed that $\boldsymbol{n}_i$ is constant in time and equal for all probes, i.e., $\boldsymbol{n}_i = \boldsymbol{n}_p$, on account of the probes being spherical and relatively close to each other.

B. State Vector

The state vector for the specific scenario consists of subvectors describing asteroid state, spacecraft state, probe states, radiation pressure constants, and bias terms:

$$\boldsymbol{X} = [\boldsymbol{X}_a^\mathsf{T}\ \boldsymbol{X}_s^\mathsf{T}\ \boldsymbol{X}_1^\mathsf{T}\ \cdots\ \boldsymbol{X}_N^\mathsf{T}\ C_{RP,s\odot}\ C_{RP,p\odot}\ \boldsymbol{n}_s\ \boldsymbol{n}_p]^\mathsf{T} \qquad (18)$$

The asteroid state is given by

$$\boldsymbol{X}_a = [\boldsymbol{r}_a^\mathsf{T}\ \dot{\boldsymbol{r}}_a^\mathsf{T}\ \mu_a]^\mathsf{T} \qquad (19)$$

i.e., position, velocity, and gravitational parameter. For the spacecraft, position, velocity, and rotation angles are stored:

$$\boldsymbol{X}_s = [\boldsymbol{r}_s^\mathsf{T}\ \dot{\boldsymbol{r}}_s^\mathsf{T}\ \boldsymbol{\psi}_s^\mathsf{T}]^\mathsf{T} \qquad (20)$$

Finally, for each probe, position and velocity are stored in addition to the coefficients for a linear model describing oscillator offset:

$$\boldsymbol{X}_i = [\boldsymbol{r}_i^\mathsf{T}\ \dot{\boldsymbol{r}}_i^\mathsf{T}\ \Delta \dot{t}_i\ \Delta t_i]^\mathsf{T} \qquad (21)$$

Note that $\Delta \dot{t}_i$ and Δt_i are only necessary for the OpRange scenario. This leads to the state vector having a total of $8N + 24$ elements with N being the number of probes.

C. Measurement Vector

The measurement vector is similarly split into subvectors for the asteroid, the spacecraft, and the probes:

$$\boldsymbol{Y} = \left[\boldsymbol{Z}_a^\mathsf{T} \boldsymbol{Z}_s^\mathsf{T} \boldsymbol{Z}_1^\mathsf{T} \cdots \boldsymbol{Z}_N^\mathsf{T} \right]^\mathsf{T} \qquad (22)$$

The asteroid measurements are the image coordinates of its center measured from the spacecraft camera:

$$\boldsymbol{Z}_a = [u_a\ \ v_a]^\mathsf{T} \qquad (23)$$

The spacecraft is observed from the tracking station with measurements consisting of two-way radar distance, ecliptic longitude and latitude measured using very long baseline interferometry (VLBI), and Doppler range rate. Also measured is the orientation of the spacecraft using the APIC platform. This leads to the following subvector:

$$\boldsymbol{Z}_s = [\rho_s\ \ \lambda_s\ \ \beta_s\ \ \dot{\rho}_s\ \ \boldsymbol{\psi}_s^\mathsf{T}]^\mathsf{T} \qquad (24)$$

Finally, for the probes, the measurement vector depends on the scenario under consideration. For OpGrav, camera coordinates and camera based ranging are used; for OpDoppler, camera coordinates and Doppler rate are used; and for OpRange, camera coordinates, radio based range, and interprobe range are used:

$$(\text{OpGrav}){:}\ \boldsymbol{Z}_i = [u_i\ \ v_i\ \ \rho_i]^\mathsf{T},$$
$$(\text{OpDoppler}){:}\ \boldsymbol{Z}_i = [u_i\ \ v_i\ \ \dot{\rho}_i]^\mathsf{T},$$
$$(\text{OpRange}){:}\ \boldsymbol{Z}_i = [u_i\ \ v_i\ \ \varrho_i\ \ \varrho_{i1}\ \ \cdots\ \ \varrho_{iN}]^\mathsf{T} \qquad (25)$$

The resulting combined measurement vectors consists of $3N + 9$, $3N + 9$, and $N(N + 2) + 9$ elements, respectively.

D. Measurement Model

The Earth-based spacecraft range measurement is calculated based on the state vector according to

$$\rho_s = |\boldsymbol{r}_s - \boldsymbol{r}_\oplus - \boldsymbol{r}_{o\oplus}| = |\boldsymbol{r}_{so}| \qquad (26)$$

where $\boldsymbol{r}_\oplus$ is the position of the Earth and $\boldsymbol{r}_{o\oplus}$ is the location of the tracking station relative to the Earth [22]. Similarly, the Doppler rate is given by

$$\dot{\rho}_s = \frac{d}{dt}|\boldsymbol{r}_s - \boldsymbol{r}_\oplus - \boldsymbol{r}_{o\oplus}| = \frac{\boldsymbol{r}_{so} \cdot \dot{\boldsymbol{r}}_{so}}{|\boldsymbol{r}_{so}|} \qquad (27)$$

and the VLBI azimuth and altitude are equal to

$$\lambda_s = \tan^{-1} \frac{r_{so,x}}{r_{so,y}} \qquad (28)$$

and

$$\beta_s = \tan^{-1} \frac{r_{so,z}}{\sqrt{r_{so,x}^2 + r_{so,y}^2}} \qquad (29)$$

respectively.

For the probes, camera coordinates are given by

$$[u_i'\ \ v_i'\ \ w_i]^\mathsf{T} = \boldsymbol{K}\boldsymbol{C}^\mathsf{T}\boldsymbol{r}_{ic}, \qquad u_i = \frac{u_i'}{w_i}, \qquad v_i = \frac{v_i'}{w_i} \qquad (30)$$

with

$$\rho_i = |\boldsymbol{r}_i - \boldsymbol{r}_s - \boldsymbol{r}_{cs}| = |\boldsymbol{r}_{ic}| \qquad (31)$$

where

$$\boldsymbol{r}_c = -\boldsymbol{C}[0\ \ 0\ \ 1]^\mathsf{T} \qquad (32)$$

is the location of the camera relative to spacecraft center of mass. $\boldsymbol{K}$ is the matrix of intrinsic camera parameters, and $\boldsymbol{C}$ is a rotation matrix that transforms from the narrow angle camera to the global frame of reference. The probe range and Doppler rate are calculated similarly to that of the spacecraft but using the spacecraft as point of reference instead of the tracking station. Interprobe distances are simply calculated as

Table 3   Measurement uncertainties (1σ)

Earth-based tracking	APIC	Radio
Spacecraft range: 1 m [22]	Asteroid direction: 0.5 pixel	Probe range: 1 m
Spacecraft Doppler: 0.1 mm/s [22]	Probe direction: 0.5 pixel	Probe Doppler: 0.03 μm/s
Spacecraft direction 1 nrad [22]	Spacecraft attitude: 2 arcsec [20]	— —

$$\varrho_{ij} = |\boldsymbol{r}_i - \boldsymbol{r}_j| + (t(\dot{\delta t}_i - \dot{\delta t}_j) + \delta t_i - \delta t_j)c \qquad (33)$$

where c is the speed of light.

For the asteroid, camera coordinates are calculated in the same way as for the probes. Table 3 shows the uncertainties associated with each type of measurement. Note that the Earth-based tracking values correspond to using 60 s samples, whereas the probe Doppler value assumes 5 s samples [30]. Further note that the APIC system has an instantaneous field of view (IFOV) of 18 μrad/pixel [20].

V.   Results

To characterize the potentially attainable performance of the mass estimation methods, in the following, the covariance analysis method has been performed with the reference trajectory set to the true value and without any noise added to the measurements or stochastic accelerations affecting the dynamics. This does not represent realistic data, but it is useful for analyzing the effects of varying different design parameters. In Sec. V.D, the impact of these simplifications will be evaluated.

Figure 5 shows the evolution of the standard deviation σ_{μ_a} of the asteroid mass estimate using the reference scenario described in Sec. II. The solid line represents OpGrav method, the dashed line represents the OpDoppler method, and the dotted line represents the OpRange method.

The initial uncertainties have been set according to Table 4. Because of the large distances and relative velocities involved in the encounter, σ_{μ_a} remains constant until just shortly before the closest approach as the deflection of the probe trajectories is negligible. During the encounter at $t = 0$, the asteroid changes the velocities of the probes by small amounts, and their paths start to diverge. The OpDoppler method quickly reaches its final precision because it measures the change in velocity directly, whereas the OpGrav and OpRange estimates gradually becomes more precise as the deviations from the undisturbed trajectories become more significant. Because
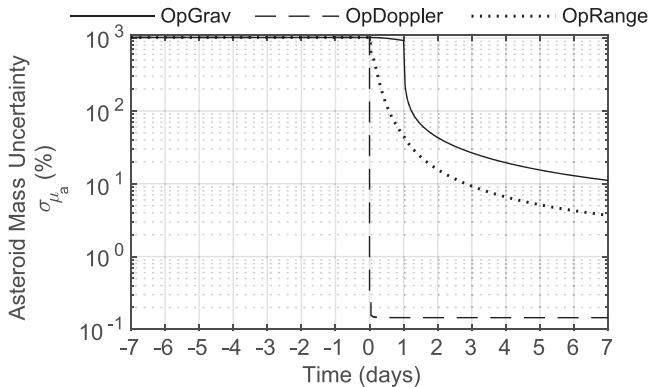
the spacecraft is focused on observing the asteroid at the closest approach, the OpGrav scenario exhibits a delayed response with the reduction in mass uncertainty only becoming evident after $t = 1$ day when the camera is redirected toward the probes.

After a period of 7 days, the probes are on average at a distance of 85 km from the spacecraft for the OpDoppler and OpRange cases and 109 km for the OpGrav case, and the magnitude of the deviation from the no-asteroid trajectories is in all instances equal to 1.3 m. The distance difference between the methods is caused by a different ejection direction being used for OpGrav, which causes the probes to travel farther before reaching the asteroid (see the next section). Even though the deflections are somewhat small compared to the distances, the estimation method is able to determine the mass of the asteroid with a 1σ precision of 3.7% for OpRange, 0.1% for OpDoppler, and 11.1% for OpGrav. Clearly, the addition of radio beacons inside the probes has a great impact on the performance of the measurement method, especially when using Doppler measurements.

To gauge the validity of the covariance analysis results, a Monte Carlo process has been performed where the state estimation algorithm was used to process 200 simulated datasets and the standard deviation of the resulting state estimates were calculated to equal 10.8, 4.2, and 0.2%, respectively, for OpGrav, OpRange, and OpDoppler with corresponding mean errors of 1.2, 0.4, and 0.1%. Good agreement with the results of the covariance analysis is observed, with the differences in precision being attributable to the relatively small sample size.

A.   Probe Parameters

1.   Effects of Ejection Parameters

Figure 6a illustrates the encounter as seen from the spacecraft and defines the probe ejection angle θ relative to the direction of travel. Changing this angle has a significant impact on the final mass uncertainty as evident from Fig. 7, especially for the OpGrav and OpDoppler cases. Note that the crosses indicate the values used in the nominal case. With reference to Figs. 6a and 6b, a probe is ejected at an angle θ relative to the spacecraft velocity vector, and in the absence of the asteroid, the probe follows the dashed line. Because of solar radiation pressure, the trajectory bends away from the sun instead of following a straight line. With the asteroid present, the probe follows the solid line, and the final position is shifted by the vector $\boldsymbol{\Delta x}$ relative to the no-asteroid case. Because of the high relative velocity of the asteroid, $|\boldsymbol{\Delta x}|$ only varies a small amount depending on ejection angle and is always located in the x-z plane. This means that for $\theta = 90$ deg the displacement will be mostly radial (maximum $|\boldsymbol{\Delta x}_r|$), whereas for

Fig. 5   Evolution of the standard deviation of the asteroid mass estimate as a function of time relative to the closest approach.

Table 4   A priori standard deviation

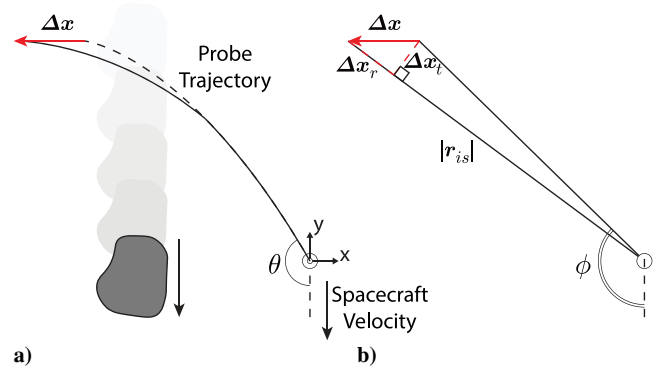| Asteroid	Spacecraft	Probe
Position: 10 km	Position: 100 m	— —
Velocity: 1 cm/s	Velocity: 1 cm/s	Ejection speed: 1 mm/s
GM: 50 m^3/s^2 $\approx$ 1000%	Attitude: 2 arcsec	Ejection angle: 0.5 deg

Fig. 6   Geometry of the asteroid encounter: a) the encounter in spacecraft-centric coordinates and b) a simplified view of the corresponding observation geometry.
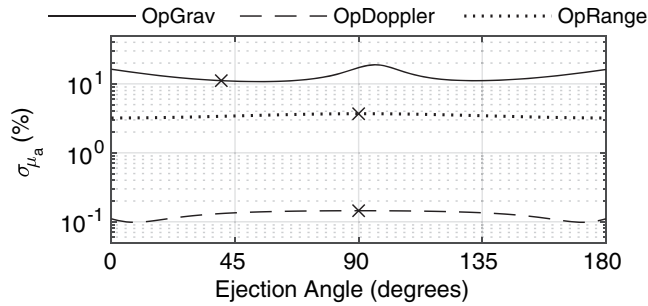
Fig. 7   Standard deviation of μ_a as a function of probe ejection angle.

Fig. 9   Standard deviation of μ_a as a function of the number of ejected probes.

$\theta = 0$ deg and $\theta = 180$ deg, the displacement will be mostly tangential (maximum $|\Delta x_t|$) as seen from the spacecraft. In addition to this, for angles close to 0 and 180 deg, the x component of the initial probe velocities will be small, resulting in longer durations between probe ejection and closest approach compared to angles close to 90 deg, which in turn leads to the spacecraft being farther away from the probes at $t = 0$. Note that the number of observations has been kept constant regardless of ejection angle.

In the OpGrav case, the tangential displacement can be better determined than the radial displacement, hence the mass uncertainty increases for angles close to 90 deg. In addition to this, the precision with which the tangential displacement can be determined decreases with range, and the mass uncertainty therefore also increases as the ejection angle approaches 0 and 180 deg.

Contrarily, the spacecraft–probe distances measured in the OpRange method contain the most information about the asteroid mass when the displacement is radial, and it would therefore be expected that the best precision should be obtained at $\theta = 90$ deg. However, the probe–probe distance measurements provide the same knowledge regardless of orientation, and the angular dependence of the OpRange method is therefore mostly constant. The slight improvement that is observed near the extreme angles can be explained by the OpRange method providing better results with increased flyby distance (see Sec. V.B.1).

The shape of the OpDoppler plot appears to be caused by variations in the uncertainty of the asteroid and spacecraft states related to the tracking geometry. Note that this effect is somewhat exaggerated in the plot on account of the logarithmic y-axis scaling.

The results in this section only deal with ejection directions lying within the encounter plane. It is quite possible that better performance can be achieved if out-of-plane directions are considered; however, this will require further analysis.

2.   Effect of Probe Mass

The effect of changing the mass of the probes is illustrated in Fig. 8. For low probe masses, the acceleration caused by solar radiation pressure will be large and will therefore cause the observation geometry to change significantly from the reference scenario. Specifically, the angle ϕ (Fig. 6b) will move toward 90 deg, and the range to the probes will increase. This, evidently, leads to a decrease in mass uncertainty, especially in the OpGrav case. Conversely, for larger probe masses, the effects of the solar radiation pressure will be less
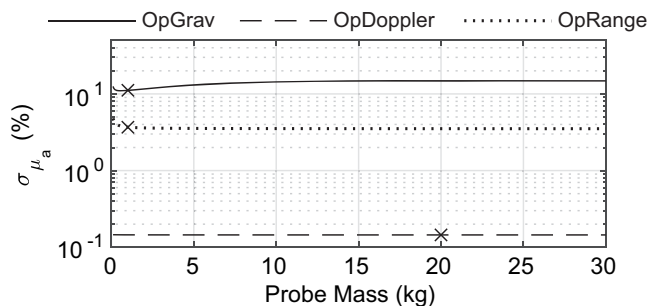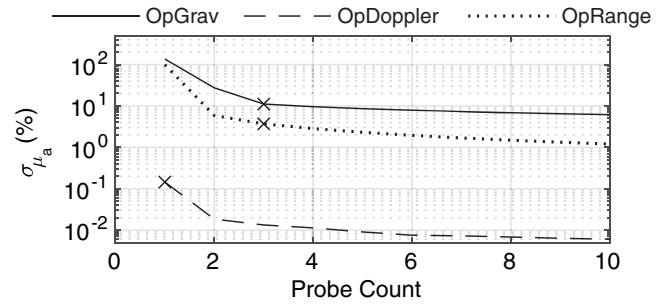
significant, and the mass uncertainty approaches a constant value, dictated by the other design parameters.

3.   Effect of Probe Count

Changing the number of ejected probes results in the mass uncertainty behavior shown in Fig. 9. With just a single probe, no meaningful mass estimation can be performed using OpGrav or OpRange because the asteroid's position is not well determined and these methods are therefore not able to decouple asteroid mass and probe distance. This is not an issue for the OpDoppler approach, which exhibits good performance using even just a single probe. Common for all, better mass estimates are obtained when more probes are used, as would be expected.

B.   Mission Parameters

1.   Effect of Orbit Design

Figure 10 displays the effect of varying the flyby distance, i.e., the minimum distance between the spacecraft and the asteroid. For the OpGrav and OpDoppler methods, a linear relationship is observed between flyby distance and mass uncertainty, as would be expected. OpRange, on the other hand, actually shows slightly improved precision at longer ranges. Considering that the precision of the radio-based measurements is modeled as being constant regardless of range, it would be expected that the mass uncertainty should be similarly constant. The improvement in mass estimation must therefore be attributed to changes in the orbital configuration. The red sections in the left part of the figure represents configurations where at least one probe was outside the field of view of the camera for a significant part of its trajectory and hence explain the associated increase in mass uncertainty.

In Fig. 11, the effect of changing the flyby speed of the spacecraft is shown, whereas the effect of varying approach distance, i.e., the minimum distance between the asteroid and the probes, is displayed in Fig. 12.

For OpDoppler and OpRange, the asteroid mass uncertainty shows simple dependence on both flyby speed and approach distance, with increased approach distance and flyby speed leading to increased mass uncertainty. This is as expected, considering that these two parameters directly affect the magnitude of probe displacement. The
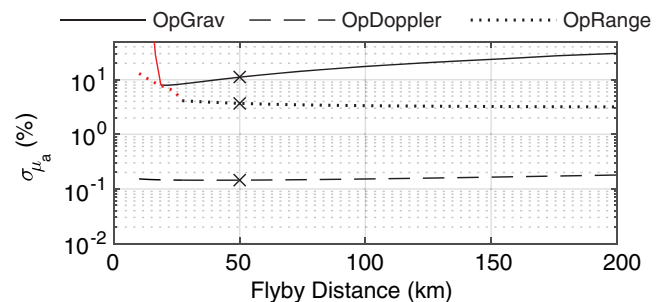

Fig. 8   Standard deviation of μ_a as a function of probe mass.

Fig. 10   Standard deviation of μ_a as a function of flyby distance. The red parts indicates probes being outside the camera's field of view.
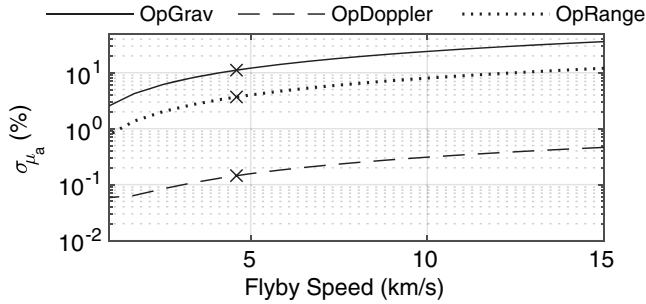
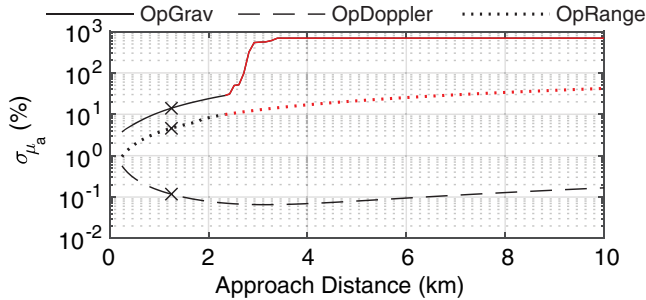Fig. 11   Standard deviation of μ_a as a function of flyby speed.

Fig. 12   Standard deviation of μ_a as a function of probe approach distance. The red parts indicate probes being outside the camera's field of view.

OpGrav case shows a more complex relation to the approach distance caused by probes being outside the field of view of the camera.

2. Effect of Asteroid Properties

Figure 13 shows how the mass estimation uncertainty varies as a function of asteroid density assuming constant volume and shape. The estimation uncertainty is observed to be inversely proportional to asteroid density. The reason for this is that the absolute value of the estimation accuracy is constant regardless of asteroid mass, thus leading to the percentile value decreasing with increasing asteroid mass and hence density. This, however, appears to not be the case for the OpDopper method, which exhibits precision proportional to asteroid density and hence produces a constant percentile value. The blue curve shows the precision obtainable using Doppler tracking of the spacecraft without launching any probes.

In Fig. 14, the dependence on asteroid diameter, assuming constant density, is displayed. Note that, in addition to changing the size of the asteroid, the approach and flyby distances were adjusted to keep the distances from the surface of the asteroid constant, assuming a spherical shape. Mass precision is shown to improve continually for all methods until a diameter of about 3 km is reached, at which point two of the probes exit the field of view of the camera. From there on, the OpGrav precision is reduced to that which can be achieved from tracking the spacecraft alone.
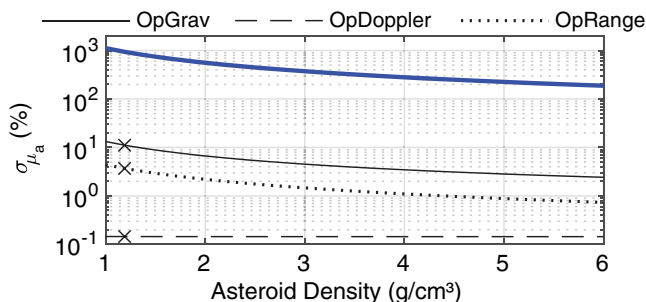

Fig. 13   Standard deviation of μ_a as a function of asteroid density. The blue line represents pure spacecraft tracking using no probes.
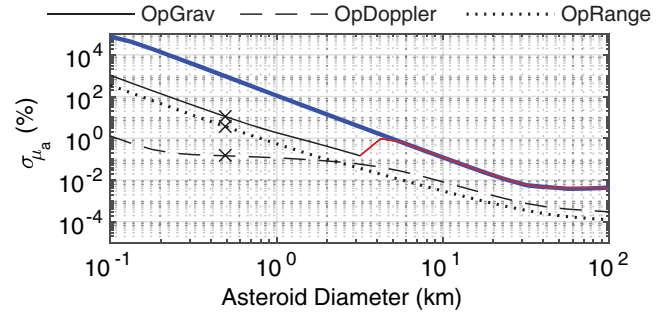

Fig. 14   Standard deviation of μ_a as a function of asteroid diameter. The red parts indicate probes being outside the camera's field of view. The blue line represents pure spacecraft tracking using no probes.

C. Measurement Parameters

Throughout this section, the measurement parameters that are not being varied use the default uncertainties presented in Table 3.

1. Effect of Earth-Based tracking

Table 5 shows the measurement uncertainties associated with spacecraft tracking at different frequency bands as well as the value of σ_{μ_a} obtained when using said bands; σ_ρ is the standard deviation of radar range, σ_I is that of the VLBI measurements, and $\sigma_{\dot\rho}$ is that of the OpDoppler measurements. Underlining indicates the values used in the nominal configuration. All three tracking systems produce nearly identical results. Clearly, the choice of tracking system has little impact on mission performance in the noiseless case.

If the positions of the asteroid and the spacecraft were both accurately determined, the mass of the asteroid could, in principle, be known from the absolute deflection of a single probe. However, because the position of the asteroid is, with an initial uncertainty of 10 km, poorly determined, the measurement principle must rely on the relative deflection of multiple probes. As a result, the absolute position of the spacecraft is not important in the calculations, and a constant σ_{μ_a} is achieved regardless of tracking system.

2. Effect of Camera Tracking

For the same reasons as for the Earth-based tracking, the absolute attitude of the spacecraft is unimportant for the mass determination process, and the mass uncertainty is constant regardless of star tracking precision. This would be subject to change if the mission parameters were modified such that the probes were not all contained in the field of view of the camera, and the spacecraft would have to reorient itself in order to image each probe. In such a case, the pointing accuracy would be expected to have a significant effect on the mass precision.

Changing the IFOV of the camera results in Fig. 15, which shows a linear dependence for σ_{μ_a} in the OpGrav case. This is expected as decreased IFOV leads to better probe trajectory determination, and the precision with which the relative positions of the probes is known completely determines the attainable mass precision.

The dependence on camera tracking precision exhibited by the OpDoppler method is caused by the decreased asteroid state uncertainty associated with better IFOV values.

Camera-based probe tracking has very little impact on the final mass uncertainty obtained with the OpDoppler and OpRange methods; however, these measurements are still needed to ensure proper convergence of the state estimation.

3. Effect of Radio Transceiver Measurements

Figure 16 shows how changing radio ranging precision affects system performance. The mass uncertainty increases with increasing range uncertainty, limited by the value set by the availability of camera measurements. Even though the range precision does not affect the OpGrav and OpDoppler methods, these are plotted as well for comparison. It can be seen that the OpRange method reaches the mass uncertainty of the OpDoppler and OpGrav methods at range precisions of approximately 0.04 and 10 m, respectively.

Table 5 σ_{μ_a} as a function of tracking system

Tracking system	σ_ρ, m	σ_I, nrad	$\sigma_{\dot\rho}$, mm/s [22]	OpGrav	OpDoppler	OpRange
S band	10	5	1	11.1%	0.1%	3.7%
X band	1	1	0.1	11.1%	0.1%	3.7%
K band	0.1	0.1	0.01	11.0%	0.1%	3.7%
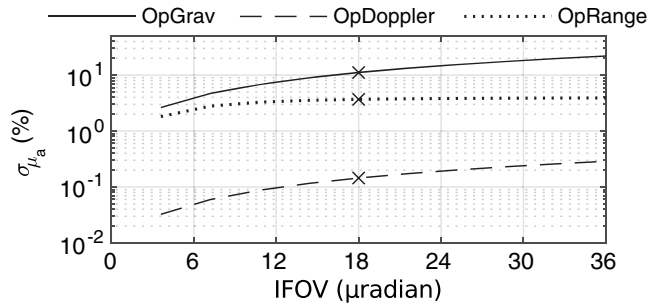
Fig. 15   Asteroid mass uncertainty as a function of camera IFOV.
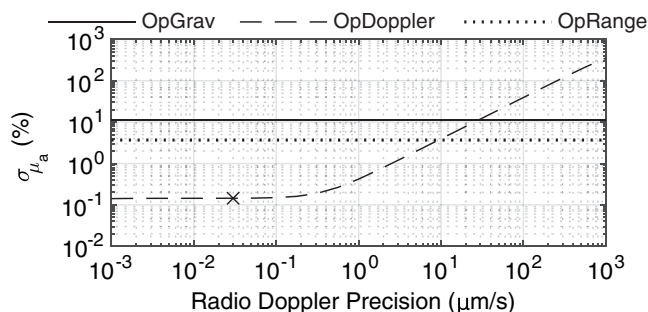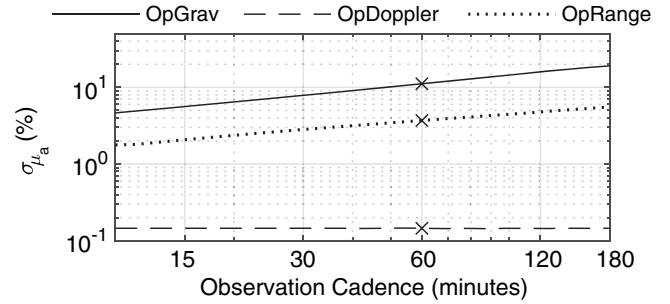

Fig. 18   Asteroid mass uncertainty as a function of observation cadence.
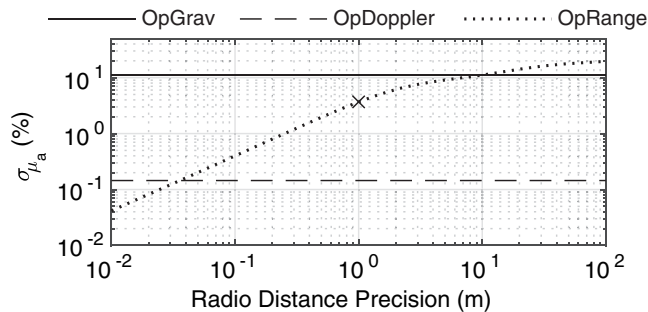
Fig. 16   Asteroid mass uncertainty as a function of probe range precision.

A similar result is obtained when varying the OpDoppler precision, as illustrated by Fig. 17. However, because only a single probe is used for the OpDoppler method, the estimation uncertainty is not as well bounded by the camera measurements and quickly reaches much higher values. The precision obtained using the OpDoppler method equals those of the OpRange and OpGrav methods at 10 and 30 μm/s, respectively.

4.   Effect of Observation Cadence

Changing the time between camera and probe range measurements changes the total number of samples for a given amount of total observation time for the OpGrav and OpRange methods. And as can be seen from Fig. 18, the value of σ_{μ_a} is therefore directly related to the time step, with shorter steps resulting in higher precision, on account of larger numbers of observations.

The reason why the observation cadence is only varied for some of the measurement types is that radiometric measurements are normally performed continuously, whereas the camera might be used

for different purposes during the mission, which will limit how often images can be captured. Similarly, probe range measurements would likely have to be spaced out in time to limit the energy storage requirements of the probes.

D.   Stochastic Effects

The results presented thus far only hold true in the case of having perfectly modeled system dynamics, which will generally not be the case in a real-world scenario. The simulations have therefore been repeated with stochastic forces added to the acceleration models of the spacecraft and the probes. For the spacecraft, exponentially correlated noise with varying noise intensities and a correlation time of 12 h has been added to the acceleration. For the probes, it is assumed that the unmodeled accelerations are equal and constant in time, and hence a random constant vector has been added for each simulation run.

Table 6 shows the results of adding the stochastic forces to the system. For the OpRange method, the process noise does not seem to affect the performance of the mass estimation by a significant amount for noise intensities below 10^{-11} km/s^2.

The OpGrav method is more sensitive to the stochastic accelerations and shows a significant increase in mass uncertainty, but it, too, levels out to a constant value.

The OpDoppler method, on the other hand, shows higher sensitivity to the noise environment and fails to produce useful results for values above 10^{-11} km/s^2. The main reason for this is that when only a single probe is used there is not enough information available to properly decouple the signal caused by the asteroid's gravity from that of other effects. While not explicitly shown here, adding additional probes to the OpDoppler scenario dramatically increases its noise robustness and causes it to behave similar to the other methods. Furthermore, because the largest error contribution is caused by uncertainty in the spacecraft state, reducing the error associated with the Earth-based tracking also significantly improves the results. Regardless, the OpDoppler method is still able to outperform the other methods for noise values of 10^{-13} km/s^2 and below.

Based on these results, it must be concluded that the OpDoppler method has the most potential, but it requires careful calibration

Fig. 17   Asteroid mass uncertainty as a function of probe Doppler precision.

Table 6   Asteroid mass uncertainty with stochastic process noise.

Noise intensity, km/s^2	OpGrav, %	OpDoppler, %	OpRange, %
10^{-14}	14.0	1.0	3.7
10^{-13}	16.3	3.2	3.7
10^{-12}	16.5	14.2	3.7
10^{-11}	16.7	111.7	3.7

and modeling to keep the process noise to a minimum. With such measures, achieving a noise level of 10^{-13} km/s^2 is possible; however, 10^{-12} km/s^2 is probably a more realistic level for most spacecraft [16].

For higher noise intensities, the OpRange method is a better choice with its more consistent performance. The OpGrav method is also capable of producing decent results in the presence of process noise, but with significantly higher uncertainty than the OpRange method.

As before, these results have been validated using Monte Carlo simulations, which showed no meaningful differences to the displayed data. For example, for a noise intensity of 10^{-14} km/s^2 the simulations resulted in standard deviations of 14.9, 1.3, and 3.3% for OpGrav, OpDoppler, and OpRange, respectively, with corresponding means of 1.5, 0.0, and 0.0%. Note that the state estimation was split into 12 h batches to accommodate the time varying nature of n_s for the Monte Carlo runs. Furthermore, the addition of probe deployment errors and stochastic acceleration will, in a real-world scenario, cause the geometry of the asteroid encounter and hence the mass estimation precision to change; however, such effects have been artificially removed to provide a more direct comparison between the covariance analysis and Monte Carlo methods.

VI. Discussion

To actually carry out a mission similar to the one described in Sec. II, there are a number of practical elements to consider.

Even though it in principle is not necessary to know the precise position of the asteroid to achieve good estimation performance, accurate knowledge is needed in order to determine the ejection time and angle which ensures optimal flyby conditions, as there otherwise is a risk that the probes will either collide with the asteroid or be too far away from it to enable precise mass estimation. The asteroid state estimate can potentially be improved by tracking it from the spacecraft before the flyby; however, process noise and ejection errors present similar issues and can severely affect the geometry of the encounter. One possible way to mitigate these issues is to eject several additional probes into a larger angular area that covers the uncertainty space, thus allowing some probes to collide with the target and some to be so far away as to not be deflected at all. This would speak for the use of the OpGrav method as it would be trivial to extend it to use more probes given the simple construction it allows for. However, such an approach would likely require a larger area to be imaged by either changing the mission parameters or adding additional cameras. Decreasing the focal length of the camera or increasing the asteroid–spacecraft distance would result in the camera covering a larger area around the asteroid (potentially at the expense of achieving the required spatial resolution on the target body) but also an increase in σ_{μ_a}, whereas adding additional cameras would increase the overall complexity of the mission. Additionally, if the probes cover too large an area, it cannot be reasonably assumed that unmodeled forces will affect them equally. Associated with adding more probes is also an increase in the mass and volume of the spacecraft, but this effect can be reduced by changing the size of each individual probe.

Another aspect that should be considered is that forces caused by the presence of potential fields or dust and gas around the asteroid (or comet) would result in the assumption of disturbances affecting all the probes evenly to not be valid. Such forces would therefore likely have to be modeled and included in the state estimation before the mass of a small body with those features can be accurately determined. Alternatively, it may be possible to lessen the impact of such disturbances by using different probe formations; however, this is likely to affect the general behavior of the mass estimation process.

At the end of the mission, the probes have an apparent brightness equivalent to a magnitude 7–8 star, assuming a 45 deg phase angle, and it should therefore not be an issue to detect them with the APIC narrow angle camera; however, this is subject to change if probe size is reduced or a different camera sensitivity is assumed. Currently, the probes reach the diffraction limit of the telescope approximately 2 days after ejection and will appear as point sources for the vast majority of the mission, which is why the 0.5 pixel should be a realistic, albeit somewhat conservative [31], estimate for the attainable probe tracking precision. The asteroid will similarly have angular extents below the

diffraction limit for the duration of the mission except for at the closest approach where it briefly will reach a diameter of approximately 400 pixels. During this critical time, it may be possible to achieve better tracking precision in theory; however, the large relative speed is likely to cause motion blur, which means that a reduction is precision is more likely. Again, 0.5 pixel should be a fair estimate of the average precision.

The value of 0.03 μm/s used for the OpDoppler measurement precision is based on the accuracy achieved by the GRAIL mission [32], which inherently means that such results are possible. However, achieving that level of precision requires advanced and extremely well-calibrated equipment and therefore represents a significant increase in complexity compared to the OpGrav scenario, especially if more than one probe has to be used in order to mitigate the process noise sensitivity. Fitting the required hardware into the probe form factor will be especially challenging, and further studies will be required to determine the feasibility.

It may seem somewhat inconsistent to use highly precise Doppler measurements but only modest camera precision in the covariance analysis. Initially, lower accuracy was used for the OpDoppler case, but this proved ineffective when faced with stochastic accelerations, and the precision was therefore improved to the current level. Because all three methods rely on camera data, decreasing the IFOV affects all of them to a similar extent. As such, the relative performance between the different methods remain approximately the same, even when the IFOV is improved significantly. The conclusions of the analysis should therefore remain valid despite this discrepancy in precision.

Achieving the 1 m range precision used in the OpRange method requires a timing precision of approximately 3 ns, which should be possible on hardware small enough to be housed inside of the probes [33]. However, for the radio beacons to adhere to the simple linear model used to describe oscillator offset, precise temperature control will be necessary. The probes will also need some sort of internal power source, as any external surface features, such as solar panels, will cause the assumption of n_p being a constant to be unrealistic. Batteries small enough to fit inside the envelope of the probes should be capable of providing sufficient power for the duration of the mission, but in general, the internal probe design will require further study.

VII. Conclusions

Three different asteroid mass estimation methods have been analyzed, all based on the concept of ejecting probes from a spacecraft performing a flyby and then tracking these probes as they pass close by the asteroid. The results have been achieved using a square root information filter based covariance analysis and verified using Monte Carlo simulations. For a Bennu-like asteroid, it has been found that its mass can be determined with a precision better than 20% using only visual tracking and better than 5% by also using radiometic measurements.

Using Doppler measurements allows for the highest accuracy and only requires a single probe, but it is sensitive to process noise and therefore requires low levels of stochastic acceleration in order to produce good results. It is also the most complicated method to implement on account of the advanced hardware needed to reach a similar precision to the GRAIL mission.

Measuring the ranges between the spacecraft and the probes as well as the ranges between the probes themselves is in general less sensitive to variations in mission parameters and process noise, but it is slightly less accurate than the Doppler based approach.

In general, the idea of using ejected probes to estimate asteroid masses is a promising concept that can significantly increase the science value of an asteroid flyby mission without adding much complexity.

Acknowledgments

Downloaded by "Arizona State University, Tempe" on April 23, 2024 | http://arc.aiaa.org | DOI: 10.2514/1.A34830

research possible as well as the Idella foundation, the Vera og Carl Johan Michaels foundation, and the William Demant foundation for helping with travel expenses. The authors also acknowledge earlier motivating discussions on this topic with S. Chesley and other colleagues at the Jet Propulsion Laboratory.

References

[1] DeMeo, F. E., Binzel, R. P., Slivan, S. M., and Bus, S. J., "An Extension of the Bus Asteroid Taxonomy into the Near-Infrared," *Icarus*, Vol. 202, No. 1, 2009, pp. 160–180.
https://doi.org/10.1016/j.icarus.2009.02.005

[2] Kochetova, O. M., "Determination of Large Asteroid Masses by the Dynamical Method," *Solar System Research*, Vol. 38, No. 1, 2004, pp. 66–75.
https://doi.org/10.1023/B:SOLS.0000015157.65020.84

[3] Baer, J., Chesley, S. R., and Milani, A., "Development of an Observational Error Model," *Icarus*, Vol. 212, No. 1, 2011, pp. 438–447.
https://doi.org/10.1016/j.icarus.2010.11.031

[4] Baer, J., Chesley, S. R., and Matson, R. D., "Astrometric Masses of 26 Asteroids and Observations on Asteroid Porosity," *Astronomical Journal*, Vol. 141, No. 5, 2011, p. 143.
https://doi.org/10.1088/0004-6256/141/5/143

[5] Baer, J., and Chesley, S. R., "Simultaneous Mass Determination for Gravitationally Coupled Asteroids," *Astronomical Journal*, Vol. 154, No. 2, 2017, p. 76.
https://doi.org/10.3847/1538-3881/aa7de8

[6] Carry, B., "Density of Asteroids," *Planetary and Space Science*, Vol. 73, No. 1, 2012, pp. 98–118.
https://doi.org/10.1016/j.pss.2012.03.009

[7] Lauretta, D. S., DellaGiustina, D. N., Bennett, C. A., Golish, D. R., Becker, K. J., Balram-Knutson, S. S., Barnouin, O. S., Becker, T. L., Bottke, W. F., Boynton, W. V., Campins, H., Clark, B. E., Connolly, H. C., Drouet d'Aubigny, C. Y., Dworkin, J. P., Emery, J. P., Enos, H. L., Hamilton, V. E., Hergenrother, C. W., Howell, E. S., Izawa, M. R. M., Kaplan, H. H., Nolan, M. C., Rizk, B., Roper, H. L., Scheeres, D. J., Smith, P. H., Walsh, K. J., Wolner, C. W. V., Highsmith, D. E., Small, J., Vokrouhlický, D., Bowles, N. E., Brown, E., Donaldson Hanna, K. L., Warren, T., Brunet, C., Chicoine, R. A., Desjardins, S., Gaudreau, D., Haltigin, T., Millington-Veloza, S., Rubi, A., Aponte, J., Gorius, N., Lunsford, A., Allen, B., Grindlay, J., Guevel, D., Hoak, D., Hong, J., Schrader, D. L., Bayron, J., Golubov, O., Sánchez, P., Stromberg, J., Hirabayashi, M., Hartzell, C. M., Oliver, S., Rascon, M., Harch, A., Joseph, J., Squyres, S., Richardson, D., Emery, J. P., McGraw, L., Ghent, R., Binzel, R. P., Asad, M. M. A., Johnson, C. L., Philpott, L., Susorney, H. C. M., Cloutis, E. A., Hanna, R. D., Connolly, H. C., Ciceri, F., Hildebrand, A. R., Ibrahim, E. M., Breitenfeld, L., Glotch, T., Rogers, A. D., Clark, B. E., Ferrone, S., Thomas, C. A., Campins, H., Fernandez, Y., Chang, W., Cheuvront, A., Trang, D., Tachibana, S., Yurimoto, H., Brucato, J. R., Poggiali, G., Pajola, M., Dotto, E., Epifani, E. M., Crombie, M. K., Lantz, C., Izawa, M. R. M., de Leon, J., Licandro, J., Garcia, J. L. R., Clemett, S., Thomas-Keprta, K., Van wal, S., Yoshikawa, M., Bellerose, J., Bhaskaran, S., Boyles, C., Chesley, S. R., Elder, C. M., Farnocchia, D., Harbison, A., Kennedy, B., Knight, A., Martinez-Vlasoff, N., Mastrodemos, N., McElrath, T., Owen, W., Park, R., Rush, B., Swanson, L., Takahashi, Y., Velez, D., Yetter, K., Thayer, C., Adam, C., Antreasian, P., Bauman, J., Bryan, C., Carcich, B., Corvin, M., Geeraert, J., Hoffman, J., Leonard, J. M., Lessac-Chenen, E., Levine, A., McAdams, J., McCarthy, L., Nelson, D., Page, B., Pelgrift, J., Sahr, E., Stakkestad, K., Stanbridge, D., Wibben, D., Williams, B., Williams, K., Wolff, P., Hayne, P., Kubitschek, D., Barucci, M. A., Deshapriya, J. D. P., Fornasier, S., Fulchignoni, M., Hasselmann, P., Merlin, F., Praet, A., Bierhaus, E. B., Billett, O., Boggs, A., Buck, B., Carlson-Kelly, S., Cerna, J., Chaffin, K., Church, E., Coltrin, M., Daly, J., Deguzman, A., Dubisher, R., Eckart, D., Ellis, D., Falkenstern, P., Fisher, A., Fisher, M. E., Fleming, P., Fortney, K., Francis, S., Freund, S., Gonzales, S., Haas, P., Hasten, A., Hauf, D., Hilbert, A., Howell, D., Jaen, F., Jayakody, N., Jenkins, M., Johnson, K., Lefevre, M., Ma, H., Mario, C., Martin, K., May, C., McGee, M., Miller, B., Miller, C., Miller, G., Mirfakhrai, A., Muhle, E., Norman, C., Olds, R., Parish, C., Ryle, M., Schmitzer, M., Sherman, P., Skeen, M., Susak, M., Sutter, B., Tran, Q., Welch, C., Witherspoon, R., Wood, J., Zareski, J., Arvizu-Jakubicki, M., Asphaug, E., Audi, E., Ballouz, R. L., Bandrowski, R., Becker, K. J., Becker, T. L., Bendall, S., Bennett, C. A., Bloomenthal, H., Blum, D., Boynton, W. V., Brodbeck, J., Burke, K. N., Chojnacki, M., Colpo, A., Contreras, J., Cutts, J., Drouet d'Aubigny, C. Y., Dean, D., DellaGiustina, D. N., Diallo, B., Drinnon, D., Drozd, K., Enos, H. L., Enos, R., Fellows, C., Ferro, T., Fisher, M. R., Fitzgibbon, G., Fitzgibbon, M., Forelli, J., Forrester, T., Galinsky, I., Garcia, R., Gardner, A., Golish, D. R., Habib, N., Hamara, D., Hammond, D., Hanley, K., Harshman, K., Hergenrother, C. W., Herzog, K., Hill, D., Hoekenga, C., Hooven, S., Howell, E. S., Huettner, E., Janakus, A., Jones, J., Kareta, T. R., Kidd, J., Kingsbury, K., Balram-Knutson, S. S., Koelbel, L., Kreiner, J., Lambert, D., Lauretta, D. S., Lewin, C., Lovelace, B., Loveridge, M., Lujan, M., Maleszewski, C. K., Malhotra, R., Marchese, K., McDonough, E., Mogk, N., Morrison, V., Morton, E., Munoz, R., Nelson, J., Nolan, M. C., Padilla, J., Pennington, R., Polit, A., Ramos, N., Reddy, V., Riehl, M., Rizk, B., Roper, H. L., Salazar, S., Schwartz, S. R., Selznick, S., Shultz, N., and Team, T. O.-R., "The Unexpected Surface of Asteroid (101955) Bennu," *Nature*, Vol. 568, No. 7750, 2019, pp. 55–60.
https://doi.org/10.1038/s41586-019-1033-6

[8] Crowe, W., Kinkaid, N., Olsen, J., and Page, J., "Spacecraft Swarm Positioning During Asteroid Flybys Using Relative Doppler and Ranging," *AIAA/AAS Astrodynamics Specialist Conference*, AIAA Paper 2016-5516, 2016.
https://doi.org/10.2514/6.2016-5516

[9] Crowe, W., Olsen, J., and Page, J. R., "Asteroid Mass Estimates from Synchronized Flybys of Multiple Spacecraft," *Journal of Guidance, Control, and Dynamics*, Vol. 41, No. 3, 2018, pp. 770–776.
https://doi.org/10.2514/1.G002907

[10] Stacey, N., and D'Amico, S., "Autonomous Swarming for Simultaneous Navigation and Asteroid Characterization," *AAS/AIAA Astrodynamics Specialist Conference*, AAS Paper 18-448, San Diego, CA, 2018.

[11] Atchison, J. A., Mitch, R. H., and Mazarico, E., "Optical Gravimetry for Flyby Missions: Parametric Study and Validation," *Lunar and Planetary Science Conference*, Lunar and Planetary Institute Paper 2308, 2017.

[12] Atchison, J. A., Mitch, R. H., Apland, C., Kee, C. L., and Harclerode, K. W., "Small Body In-Situ Multi-Probe Mass Estimation Experiment (SIMMEE)," *IEEE Aerospace Conference*, IEEE, New York, 2017, pp. 1–9.
https://doi.org/10.1109/AERO.2017.7943741

[13] Fujimoto, K., Stacey, N., and Turner, J. M., "Stereoscopic Image Velocimetry as a Measurement Type for Autonomous Asteroid Gravimetry," *AIAA/AAS Astrodynamics Specialist Conference*, AIAA Paper 2016-5566, 2016.
https://doi.org/10.2514/6.2016-5566

[14] Ledbetter, W., Sood, R., and Stuart, J., "Expected Accuracy of Density Recovery Using Satellite Swarm Gravity Measurements," *AAS/AIAA Space Flight Mechanics Meeting*, AAS Paper 19-529, San Diego, CA, 2019.

[15] Chesley, S. R., French, A. S., Davis, A. B., Jacobson, R. A., Brozović, M., Farnocchia, D., Selznick, S., Liounis, A. J., Hergenrother, C. W., Moreau, M. C., Pelgrift, J., Lessac-Chenen, E., Molaro, J. L., Park, R. S., Rozitis, B., Scheeres, D. J., Takahashi, Y., Vokrouhlický, D., Wolner, C. W. V., Adam, C., Bos, B. J., Christensen, E. J., Emery, J. P., Leonard, J. M., McMahon, J. W., Nolan, M. C., Shelly, F. C., and Lauretta, D. S., "Trajectory Estimation for Particles Observed in the Vicinity of (101955) Bennu," *Journal of Geophysical Research: Planets*, Vol. 125, No. 9, 2020, Paper e2019JE006363.
https://doi.org/10.1029/2019 JE006363

[16] Scheeres, D. J., McMahon, J. W., French, A. S., Brack, D. N., Chesley, S. R., Farnocchia, D., Takahashi, Y., Leonard, J. M., Geeraert, J., Page, B., Antreasian, P., Getzandanner, K., Rowlands, D., Mazarico, E. M., Small, J., Highsmith, D. E., Moreau, M., Emery, J. P., Rozitis, B., Hirabayashi, M., Sánchez, P., wal, S. V., Tricarico, P., Ballouz, R.-L., Johnson, C. L., Asad, M. M. A., Susorney, H. C. M., Barnouin, O. S., Daly, M. G., Seabrook, J. A., Gaskell, R. W., Palmer, E. E., Weirich, J. R., Walsh, K. J., Jawin, E. R., Bierhaus, E. B., Michel, P., Bottke, W. F., Nolan, M. C., Connolly, H. C., and Lauretta, D. S., "The Dynamic Geophysical Environment of (101955) Bennu Based on OSIRIS-REx Measurements," *Nature Astronomy*, Vol. 3, No. 4, 2019, pp. 352–361.
https://doi.org/10.1038/s41550-019-0721-3

[17] Scheeres, D., Hesar, S., Tardivel, S., Hirabayashi, M., Farnocchia, D., McMahon, J., Chesley, S., Barnouin, O., Binzel, R., Bottke, W., Daly, M., Emery, J., Hergenrother, C., Lauretta, D., Marshall, J., Michel, P., Nolan, M., and Walsh, K., "The Geophysical Environment of Bennu," *Icarus*, Vol. 276, 2016, pp. 116–140.
https://doi.org/10.1016/j.icarus.2016.04.013

[18] Klipstein, W. M., Arnold, B. W., Enzer, D. G., Ruiz, A. A., Tien, J. Y., Wang, R. T., and Dunn, C. E., "The Lunar Gravity Ranging System for the Gravity Recovery and Interior Laboratory (GRAIL) Mission," *GRAIL: Mapping the Moon's Interior*, Springer-Verlag, New York, 2013, pp. 57–76.
https://doi.org/10.1007/978-1-4614-9584-0_4

[19] Tapley, B. D., Bettadpur, S., Watkins, M., and Reigber, C., "The Gravity Recovery and Climate Experiment: Mission Overview and Early Results,"

Geophysical Research Letters, Vol. 31, No. 9, 2004, Paper L09607.
https://doi.org/10.1029/2004GL019920

[20] Park, R., and Riedel, J., "Advanced Pointing Imaging Camera (APIC) Concept," *EPSC-DPS Joint Meeting*, Europlanet Society and the AAS Division for Planetary Science, 2019, Paper EPSC-DSP2019-19.

[21] Bierman, G. J., Factorization Methods for Discrete Sequential Estimation, *Mathematics in Science and Engineering*, Vol. 128, Academic Press, New York, 1977, pp. 1–241.

[22] Park, R. S., Scheeres, D. J., Giampieri, G., Longuski, J. M., and Fischbach, E., "Estimating Parameterized Post-Newtonian Parameters from Spacecraft Radiometric Tracking Data," *Journal of Spacecraft and Rockets*, Vol. 42, No. 3, 2005, pp. 559–568.
https://doi.org/10.2514/1.7647

[23] Park, R. S., Werner, R. A., and Bhaskaran, S., "Estimating Small-Body Gravity Field from Shape Model and Navigation Data," *Journal of Guidance, Control, and Dynamics*, Vol. 33, No. 1, 2010, pp. 212–221.
https://doi.org/10.2514/1.41585

[24] Park, R. S., Asmar, S. W., Buffington, B. B., Bills, B., Campagnola, S., Chodas, P. W., Folkner, W. M., Konopliv, A. S., and Petropoulos, A. E., "Detecting Tides and Gravity at Europa from Multiple Close Flybys," *Geophysical Research Letters*, Vol. 38, No. 24, 2011, Paper L24202.
https://doi.org/10.1029/2011GL049842

[25] Park, R. S., Asmar, S. W., Fahnestock, E. G., Konopliv, A. S., Lu, W., and Watkins, M. M., "Gravity Recovery and Interior Laboratory Simulations of Static and Temporal Gravity Field," *Journal of Spacecraft and Rockets*, Vol. 49, No. 2, 2012, pp. 390–400.
https://doi.org/10.2514/1.a32117

[26] Park, R., Bills, B., Buffington, B., Folkner, W., Konopliv, A., Martin-Mur, T., Mastrodemos, N., McElrath, T., Riedel, J., and Watkins, M., "Improved Detection of Tides at Europa with Radiometric and Optical Tracking During Flybys," *Planetary and Space Science*, Vol. 112, 2015, pp. 10–14.
https://doi.org/10.1016/j.pss.2015.04.005

[27] Tapley, B., Schutz, B., and Born, G., *Statistical Orbit Determination*, Elsevier Academic Press, Burlington, 2004, pp. 159–386.
https://doi.org/10.1016/B978-0-12-683630-1.X5019-X

[28] Scheeres, D. J., Han, D., and Hou, Y., "Influence of Unstable Manifolds on Orbit Uncertainty," *Journal of Guidance, Control, and Dynamics*, Vol. 24, No. 3, 2001, pp. 573–585.
https://doi.org/10.2514/2.4749

[29] Georgevic, R. M., "The Solar Radiation Pressure Force and Torques Model." *Journal of the Astronautical Sciences*, Vol. 20, No. 5, 1973, pp. 257–274.

[30] Konopliv, A. S., Park, R. S., Yuan, D.-N., Asmar, S. W., Watkins, M. M., Williams, J. G., Fahnestock, E., Kruizinga, G., Paik, M., Strekalov, D., Harvey, N., Smith, D. E., and Zuber, M. T., "The JPL Lunar Gravity Field to Spherical Harmonic Degree 660 from the GRAIL Primary Mission," *Journal of Geophysical Research: Planets*, Vol. 118, No. 7, 2013, pp. 1415–1434.
https://doi.org/10.1002/jgre.20097

[31] Bhaskaran, S., and Kennedy, B., "Closed Loop Terminal Guidance Navigation for a Kinetic Impactor Spacecraft," *Acta Astronautica*, Vol. 103, 2014, pp. 322–332.

[32] Konopliv, A. S., Park, R. S., Yuan, D.-N., Asmar, S. W., Watkins, M. M., Williams, J. G., Fahnestock, E., Kruizinga, G., Paik, M., Strekalov, D., Harvey, N., Smith, D. E., and Zuber, M. T., "High-Resolution Lunar Gravity Fields from the GRAIL Primary and Extended Missions," *Geophysical Research Letters*, Vol. 41, No. 5, 2014, pp. 1452–1458.
https://doi.org/10.1002/2013gl059066

[33] Christensen, L., and Merayo, J., "Solution for Wireless Time Synchronization Using Sub-Nyquist Sampling Rates," *Measurement Science and Technology*, Vol. 31, No. 5, 2020, Paper 055001.
https://doi.org/10.1088/1361-6501/ab63e9

[34] Christensen, L., "Multi-Sensor Data Fusion for Spacecraft Navigation," Ph.D. Dissertation, DTU Space, Technical Univ. of Denmark, Kongens Lyngby, Denmark, 2021.

J. McMahon
Associate Editor